

# Effect of temperature and strain rate on the workability of spray formed FGH4095 superalloy in hot deformation

*The hot compression testing of hot isostatically pressed (HIPed) spray formed (SF) nickel-base superalloy was carried out in the temperature range of 1050-1150°C at strain rates of 0.001-10s<sup>-1</sup> and engineering strain of 10-70% using Gleeble-1500 thermal simulator. Transmission electron microscope (TEM) and electron backscatter diffraction (EBSD) technique were used to study the effect of strain rate on the microstructure evolution of the alloy during hot deformation. The true stress-true strain flow curve shows that the flow stress decreases with increasing deformation temperature and decreasing strain rate. Microstructure observations reveal that the dynamic recrystallization (DRX) process was stimulated at high strain rates ( $\dot{\epsilon} \geq 1 \text{ s}^{-1}$ ) due to the high dislocation density and adiabatic temperature rise. High deformation temperature and strain rate is conducive to the occurrence of dynamic recrystallization. Meanwhile, particular attention was also paid to the evolution of twin boundaries during hot deformation. It was found that there was a lower fraction of S3 boundaries at the intermediate strain rate of 1 s<sup>-1</sup>, while the fractions of S3 boundaries were much higher at both the lower strain rates ( $\dot{\epsilon} \leq 0.1 \text{ s}^{-1}$ ) and higher strain rates ( $\dot{\epsilon} \geq 4 \text{ s}^{-1}$ ). During the transformation process, the dislocations inside the subgrains and around the subgrain boundaries were annihilated by dislocation reaction and absorption.*

**Key words:** Strain rate, spray forming, nickel based superalloy, hot deformation.

## 1. Introduction

With the development of aerospace industry, the required performance of turbine disk material is more and more strict, and the alloying extent becomes higher and higher. The traditional superalloy has lots

of defects such as poor processing performance, difficulties in forming and serious segregation and they can no longer satisfy the demands of the development of modern aerospace technology. So, powder metallurgy (PM) superalloy comes into existence with the development of superalloy, which can virtually eliminate macro-segregation. FGH95 superalloy (similar to Rene 95) has wide applications in producing turbine disks, because it possesses good elevated temperature mechanical properties (Guo, Ge and Xu, 2013; Jia, Ge and Yan, 2016; Chen, Yan, Chen, Zhang, Hu and Fu, 2001). Spray forming (SF) is a novel rapid solidification technique which has been quickly developed in recent years. Currently, the preparation process of FGH95 superalloy, including powder preparation, powder pretreatment, hot isostatic pressing, etc., is complex. By contrast, spray forming can reduce the procedure and cost of production (Li, Guo, Guo, Peng and Wu, 2011; Li, Guo, Guo, Peng and Wu, 2011; Wen, et al. 2015; Galindo-Nava, Rae, 2015; Kang, Zhang, Suna, 2008; Guo, 2010; Zhang, Zhang, Jiang, Zhou, Zhao, Yang, 2015).

A great number of researches on superalloy have been carried out, however, most of them aimed at the traditional superalloy (Hesam, Mohammadi and Khalaj, 2017; He, Dong, Zhang, Zheng, Yao, 2015; Wang, Dong, Zhang, Xie, 2013; Zhou, Baker, 1994; Li, Song, Wang, Chen, 2009). In the authors' previous work (Zhang, Li, Yuan, Li, Wang, 2013; Miura, Ikeda, Iwahashi, Osada, 2010), the constitutive models for describing the hot deformation behaviour of FGH95, over a range of temperatures (1020-1150°C) and strain rates (0.001 s<sup>-1</sup> to 1s<sup>-1</sup>), was established by appropriate constitutive models. The objective of the present work is to understand the effect of strain rate on the evolution of microstructural mechanisms of the FGH4095 during hot deformation. The deformation temperature sensitivity exponent and the strain rate sensitivity exponent as important parameters have a great significance in the hot deformation.

Recently, the growth of aerospace industry becomes more and more prospective, the need of high-performance disk material is increasingly selective, and the corresponding

Messrs. Hai-Xin Wu, Min Xia, Qing-Zhi Yan, Tian Tian, Qi-Peng Hu and Chang-Chun Ge\*, University of Science and Technology Beijing, Beijing 100 083, China. \*Corresponding author (E-mail: ccge@mater.ustb.edu.cn)

extent of alloying is much higher. With respect to old super-alloy, there are many defects including relatively low performance, forming and segregation inhibition, actually they are not suitable for the high development of advanced aerospace technologies. Therefore, the application of powder metallurgy (PM) super-alloy becomes more and more widely, due to elimination of macro-segregation. The application of FGH95 super-alloy (which is similar to Rene 95) is promising for the production of turbine disks, because it owns ideal mechanical

properties according to elevated temperature (Guo, Ge and Xu, 2013; Jia, Ge and Yan 2016; Chen, Yan, Chen, Zhang, Hu and Fu, 2001). The technique of spray forming (SF) is newly developed in last several years. Nowadays, the process of preparation of FGH95 super-alloy is complex, including the following steps: preparation for powder, powder's pretreatment, hot isostatic pressing, and so on. In the contrast, the application of spray forming can simplify the procedures and reduce cost (Li, Guo, Guo, Peng and Wu, 2011; Li, Guo, Guo, Peng and Wu, 2011; Wen, Lin, Chen, Chen, Zhang, Liang, Li, 2015; Galindo-Nava, Rae, 2015; Kang, Zhang, Suna, 2008; Guo, 2010; Zhang, Zhang, Jiang, Zhou, Zhao, Yang, 2015).

A good number of scholars in the field of super-alloy did related studies, but most of the studies are focused on old super-alloy (Hesam, Mohammadi and Khalaj, 2017; He, Dong, Zhang, Zheng, Yao, 2015; Wang, Dong, Zhang, Xie, 2013; Zhou, Baker, 1994; Li, Song, Wang, Chen, 2009). According to the authors' related studies (Zhang, Li, Yuan, Li, Wang, 2013; Miura, Ikeda, Iwahashi, Osada, 2010), the models for explaining the behaviour of hot deformation of FGH95, with temperature from 1020°C to 1150°C, and rate of strain from 0.001 s-1 to 1s-1, were fixed. The aim of present study is to investigate the effects of rate of strain on the change of microstructures of FGH4095 during the process of deformation caused by heat. The rate and temperature sensitivity can largely influence the process of deformation.

## 2. Experimental material and method

Table 1 shows the chemical composition (in wt.%) of the Ni-Cr-Co based spray formed superalloy.

TABLE 1: CHEMICAL COMPOSITIONS OF THE STUDIED Ni-BASED SUPERALLOY (WT.%).

C	Cr	W	Mo	Al	Ti	Nb	B	Co
0.04-0.09	12.00-13.00	3.00-4.00	3.00-4.00	3.00-4.00	3.00-4.00	1.00-2.00	0.006-0.01	6.00-8.00
Al	Mn	Si	Mg	Fe	P	S	Zr	Ni
3.00-4.00	0.15	0.05	0.001-0.004	0.20-0.30	0.01-0.0	0.001-0.005	0.03-0.07	Bal

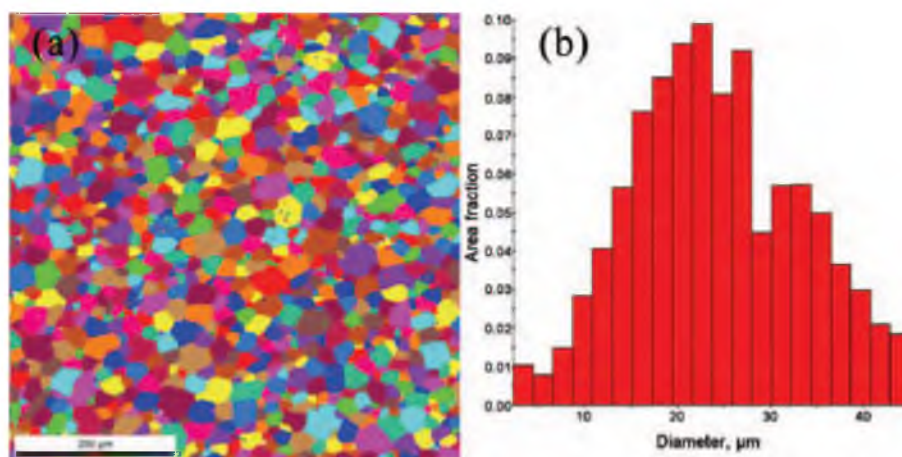


Fig.1 EBSD IPF image and grain size distribution of the as-received alloy FGH4095

Chemical composition of Ni-Cr-Co-based spray formed super-alloy (in wt.%) is shown in Table 1.

Fig. 1 shows the microstructure and grain size distribution of the as-received alloy FGH4095 before compression tests. The morphology shows remarkably spherical or quasi-spherical grains and the grain size in the range of 10 μm to 40 μm, with an average grain grade of about ASTM 7~8.

Hot compression tests were conducted using a Gleeble-1500 thermal simulator at the temperatures of 1050°C, 1080°C, 1110°C and 1150°C and in the strain rates of 0.01 s-1, 0.1 s-1, 1 s-1 and 10s-1 with 10 mm diameter, 15 mm high cylindrical specimens. All specimens were heated to the deformation temperatures at a heating rate of 10°C/s and held for 2 mins in order to gain the uniform microstructure before the hot compression test. The load-stroke data obtained in compression were processed to obtain true stress-true strain curves using standard equations. Grain sizes were determined according to ASTM E112 linear intercept procedures using circular grid overlays. The samples for EBSD investigation were mechanically polished and then polished electrolytically in a 20% H2SO4+80% methanol solution at 30 V for about 6 min at room temperature. The EBSD measurement was conducted on a LEO1450 scanning electron microscope equipped with INCA Channel 5 software. The orientation imaging microscopy (OIM) maps and misorientation angle of grains and sub-grains were calculated from the EBSD results. The foils for TEM observation were prepared by hand grinding to a thickness of 60 mm. Discs of 3 mm in diameter were punched from the thin slice and then thinned using twinjet electropolishing with a solution of 5% perchloric acid in ethanol. TEM examination was conducted with Tecnai G2

F30 S-TWIN transmission electron microscope operated at 300 kV.

The microstructures of alloy FGH4095 along with corresponding size distribution is shown in Fig.1. The morphology proves the existence of spherical or quasi-spherical grains, at the same time, the grain size is from 10  $\mu\text{m}$  to 40  $\mu\text{m}$ , with an average grade of ASTM 7~8.

The tests of hot compression were carried out through a thermal simulator of Gleeble-1500 under the temperatures: 1050°C, 1080°C, 1110°C and 1150°C, and with the rates of strain: 0.01 s<sup>-1</sup>, 0.1 s<sup>-1</sup>, 1 s<sup>-1</sup> and 10 s<sup>-1</sup>, the diameter is 10mm, 15mm the high of cylindrical specimens is 15mm. To obtain the uniform microstructure before compression test, the rate for heating is fixed at 10°C/s, and the period of hold is about 2 mins. Load-stroke data gained in the process of compression were analyzed to figure out the stress-true strain curves of strain via standard formulas. The sizes of grain were fixed with respect to the procedures of ASTM E112 linear intercept via overlays of circular grid. The samples applied for EBSD study were polished via mechanical approach, and then further polished electrically in a solution of 20% H<sub>2</sub>SO<sub>4</sub>+80% methanol at 30 V at room temperature for around 6 minutes. EBSD measurement process was carried out via a LEO1450 electron scanning microscope installed with the software of INCA Channel 5. The orientation angle of grains and sub-grains as well as the orientation imaging microscopy (OIM) maps were figured out through EBSD results. The foils grinding to a thickness of 60 nm for TEM were figured out by hand. Discs with 3-mm diameter were punched from the thin slice and then thinned via twinjet electro-polishing using a solution of 5% perchloric acid - ethanol. TEM test was carried out with a Tecnai G2 F30 S-TWIN transmission electron microscope of 300 kV.

### 3. Experimental result discussions

#### 3.1. FLOW STRESS-STRAIN CURVES

The Fig.2 shows the true stress-true strain curves of the spray formed superalloy recorded at various temperatures from 1050 to 1150°C under strain rates from 0.001 s<sup>-1</sup> to 10 s<sup>-1</sup>. A typical flow stress curve is composed for three stages: stage 1 (work hardening stage), the stress increases rapidly with increasing strain; stage 2 (softening stage), the stress decreases when peak stress reached; stage 3 (steady stage), the stress almost unchanged. In the stage 1, because of work hardening and dynamic recovery, the dislocation density

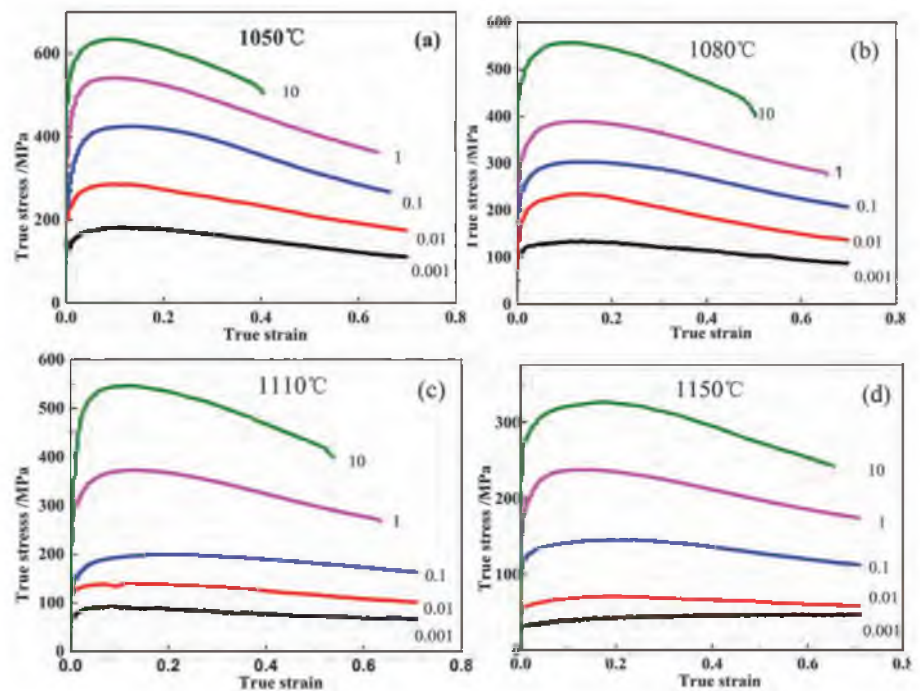


Fig.2 True stress-true strain flow curve at (a) 1050°C (b) 1080°C (c) 1110°C (d) 1150°C

increase and the formation of poorly developed sub-grain boundaries, so the stress increases rapidly. The high dislocation density stimulates the occurrence of dynamic recrystallization once a critical strain is exceeded, then the flow stress decreases which means the coming of stage 2. In this stage, the dislocations are annihilated in large numbers through the migration of a high angle boundary and the stress drops steeply. Finally, because of a new balance between softening and hardening, it enters the stage 3.

We can also find some regular rules from the Fig.2. For a constant deformation temperature, higher the strain rate is, the higher is the flow stress. Because higher strain rate provides shorter time for energy accumulation and dynamic recrystallization cannot occur completely. Thereby, it increases the critical shear stress for starting the slip systems during hot deformation, and resulting in the increase of flow stress. So, the effect of deformation temperature and strain rate on flow stress can be explained by the terms of dynamic recrystallization and dislocation mechanism. For a constant strain rate, the lower the deformation temperature is, the higher is the flow stress. Because with the increase of deformation temperature, the atoms in the superalloy become more active, the binding force between atoms decreases and more slip systems start. The dislocations also become more active which means they can overcome the pinning effect and accomplish the activities such as the cross-slip of screw dislocation and the climb of edge dislocation. Meanwhile the nucleation rate and growth rate of dynamic recrystallized grain also increase, so the softening effect strengthens, leading to the decrease of flow stress.

The true curves of spray formed super-alloy are shown in Fig.2, the temperature range is from 1050°C to 1150°C, the rates of strain is from 0.001 s<sup>-1</sup> to 10s<sup>-1</sup>. Usually a common flow stress curve can be divided into three stages: stage 1: work hardening stage, during which the stress will increase very rapidly with strain; stage 2: softening stage, during which the stress decreases after reaching the peak value; stage 3: steady stage, during which the stress is stable. In stage 1, due to hardening and dynamical recovery, the density of dislocation increases, and the sub-grain boundaries are developed poorly, that explains why the increase of stress is at high rate. High density of dislocation mimics the process of dynamic recrystallization once a standard strain is overpassed, and then flow stress will decrease indicating the start of stage 2. During this stage, the dislocations are restrained in large amounts via the move of a high-angle boundary and the stress decreases steeply. Finally, due to a new balance between softening and hardening, stage 3 starts.

Some rules can be found from Fig.2. For deformation under constant temperature, the flow stress increases with the rate of strain. The reason is that higher rate requires smaller amount of time for accumulation of energy, and dynamical recrystallization cannot be realized completely. Therefore, the critical shear stress is increased for starting the slip systems for the process of deformation caused by heating, leading to increase of the flow stress. The effects produced by temperature and rate of strain on flow stress can be understood via dynamical recrystallization and dislocation rules. With a constant rate of strain, the lower the temperature is, the higher is the flow stress. The reason is that as the temperature increases, the atoms of super-alloy become more physically active, due to the fact that the binding between atoms becomes weak, indicating the start of slip systems. The dislocation accordingly becomes active indicating that they can overcome the inhibition of pinning effect and realize the following activities: cross-slip of screwed dislocation and climb of edged dislocation. In the meanwhile, the nucleation rate as well as the growth rate of dynamic recrystallized grain increases too, therefore the softening effects are strengthened, followed by the decrease of flow stress.

### 3.2. EFFECT OF STRAIN RATE ON THE MICROSTRUCTURE EVOLUTION

#### 3.2.1. Microstructure evolution

Fig.3 shows the orientation imaging microscopy (OIM) maps of specimen compressed to a true strain of 0.5 at 1150°C with different strain rates. The S3, S9 and S27 boundaries are respectively marked by red, green and blue lines. From Fig.3, it can be easily found that the grain microstructures are significantly affected by strain rate. It can be seen that a large number of twins have the S3 twin relationship. Under the relatively high strain rate ( $\dot{\epsilon} = 10$ ), there are some serrated grain boundaries, as shown in Fig. 3 (a).

It is observed that small dynamic recrystallized grains

grow near the old grain boundaries, indicating that the grain boundaries are the favourable sites for the nucleation of DRX grain. When the strain rate is decreased to 0.3, small DRX grains appear on the initial grain boundaries and tend to completely occupy the initial grain boundaries. With the further straining, the previous DRX grains obviously grow up, as shown in Fig.3 (b) and (c). Under relatively low strain rate ( $\dot{\epsilon} = 0.01$  and  $\dot{\epsilon} = 1E-3$ ), the uniform equiaxed fine DRX grains appear, as shown in Fig.3(d) and (e), indicating that the dynamic recrystallization is finished. Therefore, it can be found that the number of DRX grains increases with the increase of deformation degree.

Orientation imaging microscopy (OIM) maps of specimen are shown in Fig.3, compressed to a strain of 0.5 under temperature of 1150°C at different rates of strain. S3, S9 and S27 boundaries are indicated by red, green and blue lines respectively. We can see from Fig.3 that, the grain microstructures significantly depend on the rate of strain. And also, many twins have S3 correlation. At relatively high rate of strain ( $\dot{\epsilon} = 10$ ), there exists some serrated boundaries, which can be seen from Fig.3(a). It can be observed that small dynamically recrystallized grains concentrate nearby the old boundaries, implying that the corresponding grain boundaries are favourable for nucleation of DRX grain. As the rate of strain decreased to 0.3, small DRX grains concentrate on the initial boundaries and even completely occupy these boundaries. With continuous straining, it is obvious that the previous DRX grains grow up, which can be seen from Fig.3(b) and (c). At relatively low rate of strain ( $\dot{\epsilon} = 0.01$  and  $\dot{\epsilon} = 1E-3$ ), the uniform equiaxed fine DRX grain appear, which can be seen from Fig.3(d) and (e), indicating the end of dynamic recrystallization. Therefore, we can see that the number of DRX grains increases with the deformation degree.

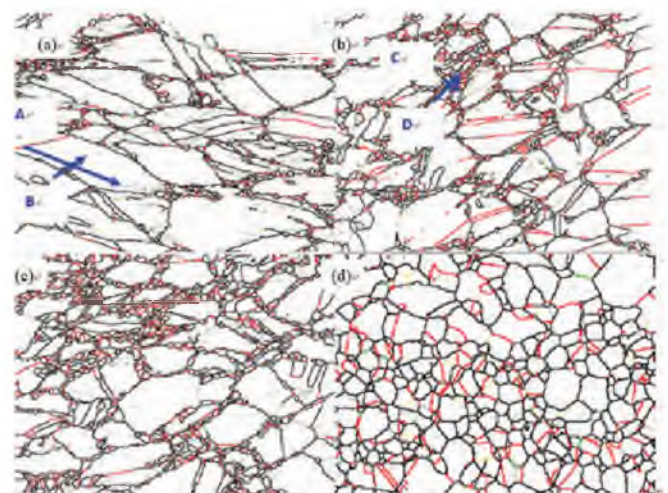


Fig. 3 OIM maps of the as-homogenized alloy deformed to different true strain at 1150°C with the strain of 0.5, (a)  $\dot{\epsilon} = 10$ ; (b)  $\dot{\epsilon} = 1$ ; (c)  $\dot{\epsilon} = 0.1$ ; (d)  $\dot{\epsilon} = 0.01$ ; (e)  $\dot{\epsilon} = 1E-3$

The variations of S3n (n = 1, 2, 3) boundaries with strain rate is shown in Fig.4., which reveals that the strain rate has a complex influence on the twin boundaries. From Fig.4., it can be found the fractions of S3 boundaries are higher at the lower strain rates ( $\dot{\epsilon} \leq 0.1 \text{ s}^{-1}$ ) and the higher strain rates ( $\dot{\epsilon} \geq 4 \text{ s}^{-1}$ ) for the alloy during hot deformation. Videlicet, the fraction of S3 boundaries at 1 s-1 is noticeably lower, indicating a weak evolution of twins at an intermediate strain rate. At the lower strain rates ( $\dot{\epsilon} \leq 0.1 \text{ s}^{-1}$ ), there is more available time for grain boundary migration, and it can enhance the growth during DRX process, resulting in the higher fraction of S3 boundaries.

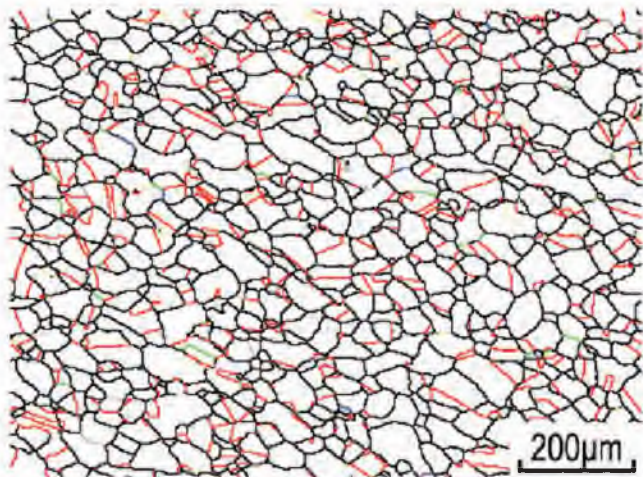


Fig.4 Variations of S3n (n = 1, 2, 3) boundaries with strain rate

Furthermore, the fraction of twins formed by growth accidents is also closely related to the driving force for grain boundary migration, and the higher stored energy can facilitate the nucleation of twins (Wang, Shao, Zhen, Yang, Zhang, 2008). In other words, the higher stored energy can also increase the frequency of growth accidents, which is favourable for the formation of twins. At the higher strain rates ( $\dot{\epsilon} \geq 4 \text{ s}^{-1}$ ), the stored energy is higher in the alloy, resulting in the higher fraction of S3 boundaries. Due to the higher fractions of twin boundaries at the lower and higher strain rates, the effect of twins on accelerating the DRX kinetics would be more significant comparing to the intermediate strain rate of 1 s-1. On the other hand, the evolutions of S9 and S27 boundaries with strain rate are similar to the S3 boundaries, due to the interactions between S3n boundaries.

The variations of boundaries for S3n (n = 1, 2, 3) are shown in Fig.4., which proves that the rate of strain has a complicate effect on twin boundaries. Through Fig.4., we can see that both the lower rate ( $\dot{\epsilon} \leq 0.1 \text{ s}^{-1}$ ) and higher rate ( $\dot{\epsilon} \geq 4 \text{ s}^{-1}$ ) contribute to the higher the fraction of S3 boundaries, for the alloy during deformation caused by heating. Lower fraction of S3 boundaries: 1 s-1, implies a weak

evolution of twins at an intermediate rate of strain. Lower rates ( $\dot{\epsilon} \leq 0.1 \text{ s}^{-1}$ ) of strain indicate more available time for boundary migration, and it can promote the growth during the process of DRX, ending with higher fraction of S3 boundaries.

What is more, the fraction of twins produced via growth accidents is correlated to driving force according to boundary migration, and the nucleation of twins can be facilitated by the higher stored energy (Wang, Shao, Zhen, Yang, Zhang, 2008). Put it in another way, the higher energy is crucial for the improvement of probability of growth accidents, which promotes the formation of twins. At higher rates ( $\dot{\epsilon} \geq 4 \text{ s}^{-1}$ ) of strain, the higher stored energy in the alloy, is responsible for the higher fraction of S3 boundaries. Therefore, the effects of twins on strengthen the kinetics of DRX become more important, according to the intermediate rate of strain at 1 s-1. Put it in another way, the evolutions of S9 and S27 boundaries are similar to that of S3 boundaries, because of the mutual interactions between S3n boundaries.

In order to further investigate the effect of CDRX at low strain rate, disorientation analysis was performed along the lines in Fig.3. As shown in Fig.5, it can be found that the point-to-point disorientations (red line) cannot exceed 3°, also the cumulative disorientations (point-to-origin disorientations, blue line) can hardly exceed 10° both near the

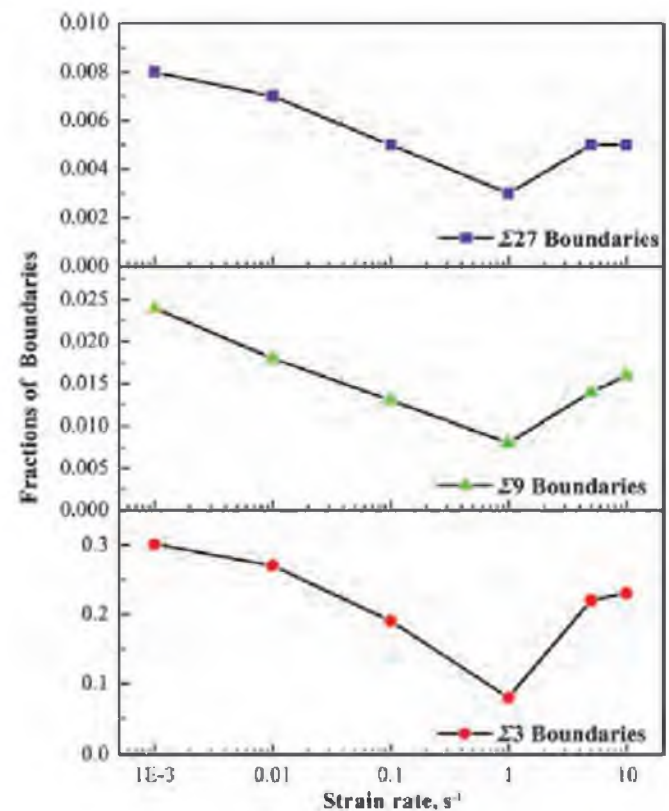


Fig.5 Disorientations measured along the lines marked in Fig.3: (a) A, (b) B, (c) C, (d) D

original grain boundaries and within the grains under the various true strains ranging from 0.1 to 0.7, implying that the progressive sub-grain merging and rotation grows weaker at low strain rate. The results further indicate that the CDRX characterized by progressive sub-grain merging and rotation plays a small role during deformation.

To further investigate the role played by CDRX at low rate of strain, disorientation analysis was carried out along the lines of Fig.3., which can be seen from Fig.5. We can see that the point-to-point disorientations (red line) are limited by the value of  $3^\circ$ , and the cumulative disorientations (point-to-origin disorientations, blue line) are limited by the value of  $10^\circ$ , both nearby the original boundaries and within the grains under different strains: from 0.1 to 0.7, indicating that merging and rotation the progressive sub-grain are weaker at lower rate. The findings further imply that the CDRX accompanied with progressive sub-grain merging and rotation, has small influence on deformation.

### 3.2.2. The nucleation mechanisms of DRX

To further analyze the DRX mechanism and microstructure evolution, the typical TEM micrographs and the selected area diffraction patterns (SADPs) obtained at  $1150^\circ\text{C}$  with the strain rate of  $0.01\text{ s}^{-1}$  in FGH4095 are shown in Fig.6. Fig.6(a) reveals that the distribution of dislocations is intensive and numerous dislocation networks appear. A new grain in Fig.6(b) grows by phagocytosing contiguous cell structures which contain a much higher dislocation density. Dislocations are present in the new grain, which indicates that it has been developed by DRX (Chen, Lin, Chen, Li, Wen, Zhang, et al., 2015).

Fig.6(c) shows the triple junction grain boundary. The concentration of stress can be liberated by the process of DRX at the triple junction grain boundary (Tao, Jia, Liu, 2010). It can be found that the dislocation densities in different grains are different. The prior study indicates that the growth of DRX grain is along with deformation which restrains the new grain and aggrandize dislocations in it (Cao, Di, Misra, Yi, Zhang, Ma, 2014). As a result, the dislocation densities in DRX grains are multiple and change with their extent of strain. Twin can be observed in the specimen as shown in Fig.6(d), as well as the selected area diffraction pattern (SADP) of the matrix and twin. The twins deriving from near the original grain boundaries can speed up the bulging as well as the

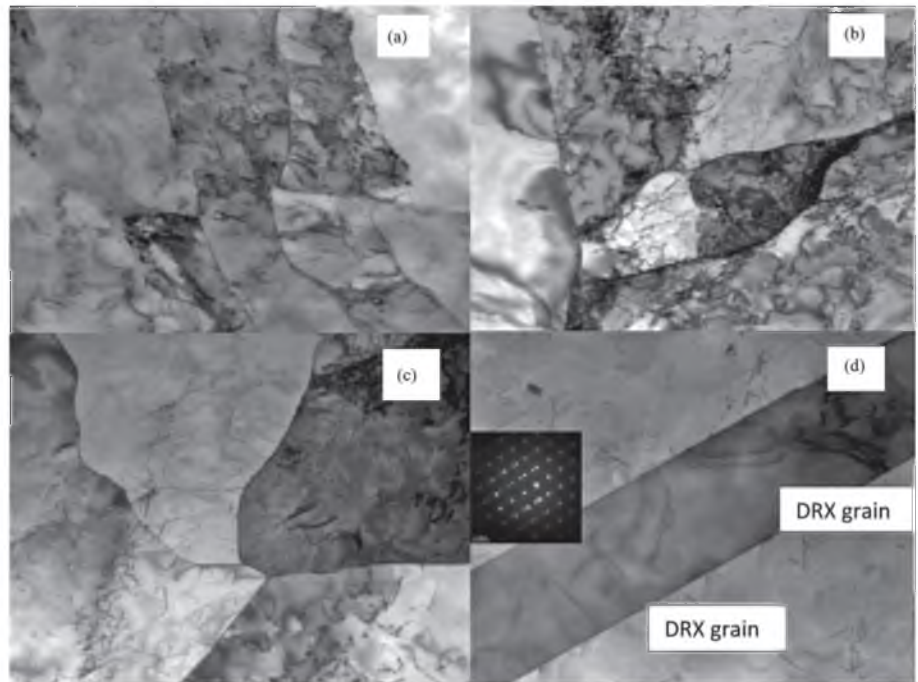


Fig.6 TEM micrographs obtained at different true strains with the temperature of  $1150^\circ\text{C}$  and the strain rate of  $0.01\text{ s}^{-1}$  in as-homogenized alloy: (a)the dislocations,  $\varepsilon=0.1$  (b) DRX nuclei formed at triple junction grain boundary,  $\varepsilon=0.3$  (c) the bulging grain boundary,  $\varepsilon=0.5$  (d) twin grain boundary and [011] SADP of the matrix and twin,  $\varepsilon=0.7$

separation of bulged parts from the primary grains, accelerating the nucleation and development of DRX grains (Wang, et al., 2014). The existing of bulging primary grain boundaries following twinning further illuminate that the dominant nucleation mechanism of DRX in FGH4095 is DDRX (Wang, Shao, Zhen, Yang, Zhang, 2008; Zhang and Zhang, 2006).

In order to further investigate the mechanism of DRX as well as the evolution of microstructure, Fig.6 shows the TEM micrographs as well as the selected area diffraction patterns (SADPs) gained under  $1150^\circ\text{C}$  with the rate of strain at  $0.01\text{ s}^{-1}$ . We can see from Fig.6(a) that the distribution of dislocation is intensive and there are lots of network of dislocation. From Fig.6(b), we can see that a new grain grows via phagocytosing contiguous cells, which owns a higher density of dislocation. Dislocations appear in new grain, indicating that it is activated by DRX (Chen, Lin, Chen, Li, Wen, Zhang, et al. 2015). The triple junction grain boundary was shown in Fig.6(c), in which the concentration of stress can be liberated via DRX (Tao, Jia, Liu, 2010). We can see that the densities of dislocation vary from grains.

The previous study implies that the growth of DRX grain follows the process of deformation, which inhibits the formation of new grain and aggrandizes the dislocations in new grain (Cao, Di, Misra, Yi, Zhang, Ma, 2014). Therefore, the densities of dislocation in DRX grains are different and the fluctuations depend on the degree of strain. As shown in

Fig.6(d) twins as well as the SADP (selected area diffraction pattern) can be observed. The twins of the original boundaries can enhance bulging and separation of bulged parts from primary grains, further promoting the process of nucleation and growth of DRX grains (Wang, Brisset, Helbert, Solas, Drouelle, Mathon, et al., 2014). The existence of bulging boundaries further explains that the main mechanism of nucleation of DRX in FGH4095 is DDRX (Wang, Shao, Zhen, Yang, Zhang, 2008; Zhang, Zhang, 2006).

#### 4. Conclusions

The following conclusions have been drawn from the results of this investigation:

- (1) The true stress-true strain curves of the spray formed superalloy shows the typical characteristics of dynamic recovery and dynamic recrystallization. The flow stress decreases with increasing deformation temperature and decreasing strain rate. The flow stress represents as the characteristic of dynamic crystallization with the increasing of strain rates higher than 0.001s<sup>-1</sup>.
- (2) The fraction of  $\Sigma 3$  boundaries increased linearly with the increasing volume fraction of DRX grains, indicating that majority of  $\Sigma 3$  boundaries were formed in the DRX process by growth accidents. Moreover, there was a sluggish evolution of  $\Sigma 3$  boundaries at an intermediate strain rate of 1 s<sup>-1</sup>, and the fractions of  $\Sigma 3$  boundaries were higher at both the lower strain rates ( $\dot{\epsilon} \leq 0.1 \text{ s}^{-1}$ ) and higher strain rates ( $\dot{\epsilon} \geq 4 \text{ s}^{-1}$ ). On the other hand, the evolutions of R9 and R27 boundaries with strain rate were similar to the  $\Sigma 3$  boundaries, due to the interactions between  $\Sigma 3n$  boundaries.
- (3) The nucleation mechanisms of DDRX and CDRX occurred simultaneously in the alloy during hot deformation, which were closely related to the strain rate. It was found that DDRX was the primary nucleation mechanism of DRX for the alloy during hot deformation, and CDRX can only be considered as an assistant one. Moreover, the effect of DDRX was firstly weakened and then strengthened with the increasing strain rate. Meanwhile, the effect of CDRX was firstly strengthened and then weakened with the increasing strain rate.
- (4) The existence of original grain boundaries bulging accompanied with twinning indicates that the dominant nucleation mechanism of DRX in FGH4095 is DDRX. CDRX nearby serrated grain boundaries occurs with DDRX, which is an ancillary nucleation mechanism.

#### Acknowledgements

This study was granted by National Natural Science Foundation of China (NSFC) 51171016.

#### References

1. Guo, B., Ge, C. C. and Xu, Y. (2013): "Flow behavior and numerical simulation of Spray Formed FGH95 superalloy under hot compression." *Iron Steel*, 20(12), pp. 69-74.
2. Jia, C. L., Ge, C. C. and Yan, Q. Z. (2016): "Microstructure evolution and mechanical properties of disk superalloy under multiplex heattreatment." *Materials Science and Engineering: A*, 659, pp. 287-294.
3. Chen, Z. H., Yan, H. G., Chen, G., Zhang, F. Q., Hu, Z. X. and Fu, J. X. (2001): "Principle and setups of multi-layer spray deposition technology." *J Hunan Univ (Nat Sci)*, 28(5), pp.20-32.
4. Li, D., Guo, Q., Guo, S., Peng, H. and Wu, Z. (2011): "The microstructure evolution and nucleation mechanisms of dynamic recrystallization in hot-deformed Inconel 625 superalloy," *Materials & Design*, 32, pp. 696-705.
5. Li, D., Guo, Q., Guo, S., Peng, H. and Wu, Z. (2011): "The microstructure evolution and nucleation mechanisms of dynamic recrystallization in hot-deformed Inconel 625 superalloy," *Materials & Design*, 32, pp. 696-705.
6. Wen, D.-X. et al. (2015): "Work hardening behaviors of typical solution-treated and aged Ni-based superalloys during hot deformation." *Journal of Alloys and Compounds*, 618, pp. 372-379.
7. Galindo-Nava, E. I. and Rae, C. M. F. (2015): "Microstructure evolution during dynamic recrystallisation in polycrystalline nickel superalloys," *Materials Science and Engineering: A*, 636, pp.434-445.
8. Kang, F. W., Zhang, G. Q. and Suna, J. F. (2008): "Hot deformation behavior of a spray formed superalloy." *Journal of materials processing technology*, 20(4), pp.136- 147.
9. Guo, J. T. (2010): *Materials Science and Engineering for Superalloy (2vols): Superalloy Materials and Engineering Applications*. Beijing: Science Press.
10. Zhang, H. B., Zhang, K. F., Jiang, S. S., Zhou, H. P., Zhao, C. H. and Yang, X. L. (2015): "Dynamic recrystallization behaviour of a g'-hardened nickel-based superalloy during hot deformation." *Journal of Alloys and Compounds*, 623, pp. 374-385.
11. Pouraliakbar, Hesam, Jandaghi, Mohammad Reza, Javad, Seyyed, Baygi, Mohammadi and Khalaj, Gholamreza (2017): "Microanalysis of crystallographic characteristics and structural transformations in SPDed Al-Mn-Si alloy by dual-straining." *Alloy Compd.*, 696, pp. 1189-1198.
12. He, J., Dong, J-X., Zhang, M., Zheng, L. and Yao, Z-C. (2015): "Hot deformation characteristics of Alloy 617B nickel-based superalloy: A study using processing map." *Journal of Alloys and Compounds*, 647, pp. 338-350.
13. Wang, J., Dong, J., Zhang, M. and Xie, X. (2013): "Hot working characteristics of nickel-base superalloy 740H during compression," *Materials Science and*

*Engineering: A*, 566, pp. 61-70.

14. Zhou, L. and Baker, T. (1994): "Effects of strain rate and temperature on deformation behaviour of IN 718 during high temperature deformation," *Materials Science and Engineering: A*, 177, pp. 1-9.
15. Li, H. Y., Song, X. P., Wang, Y. L. and Chen, G. L. (2009): "Stability of  $\gamma'$  phase in FGH95 superalloy." *Eng Rare Met Mater.*; 38(1), pp.64-72.
16. Zhang, M. J., Li, F. G., Yuan, Z. W., Li, J. and Wang, S. Y. (2013): "Effect of heat treatment on the microindentation behavior of powder metallurgy nickel based superalloy FGH96," *Materials & Design*, 49, pp.705-715.
17. Miura, H., Ikeda, H., Iwahashi, T. and Osada, T. (2010): "High temperature and fatigue properties of injection moulded superalloy compacts." *Powder Injection Moulding Inter* 4, 68-70.
18. Guo, Q., Li, D., Peng, H., Guo, S., Hu, J. and Du, P. (2012): "Nucleation mechanisms of dynamic recrystallization in Inconel 625 superalloy deformed with different strain rates," *Rare Metals*, 31, pp. 215-220.
19. Kumar, S. S. S., Raghu, T., Bhattacharjee, P. P., Rao, G. A. and Borah, U. (2016): "Strain rate dependent microstructural evolution during hot deformation of a hot isostatically processed nickel base superalloy," *Journal of Alloys and Compounds*, 681, pp.28-42.
20. Semiatin, S. L., McClary, K. E., Rollett, A. D., Roberts, C. G., Payton, E. J., Zhang, F. and Gabb, T. P. (2013): "Plastic flow and microstructure evolution during thermomechanical processing of a PM nickel-base superalloy," *Metallurgical and Materials Transactions A*, 44, pp. 2778-2798.
21. Semiatin, S. L., Shank, J. M., Shiveley, A. R. and Saurber, W. M., Gausa, E. F. and Pilchak, A. L. (2014): "The effect of forging variables on the supersolvus heat treatment response of powder metallurgy nickel base superalloys," *Metallurgical and Materials Transactions A*, 45, pp. 6231-6251.
22. Stephen, P., Coryell, Kip O., Findley, Martin and Mataya, C. (2010): "Flow Behavior of Superalloy 945 During High Temperature Deformation." *The Minerals Metals & Materials Society*, 20 (1), pp. 291-299.
23. Tao, Y., Jia, J. and Liu, J.T.(2010): "Microstructure characterization and mechanical properties of FGH 95 turbine blade retainers," *J Iron Steel Res Int.*, 17(9), pp.73-85.
24. Wang, W., Brisset, F., Helbert, A., Solas, D., Drouelle, I. and Mathon, M. et al. (2014): "Influence of stored energy on twin formation during primary recrystallization," *Materials Science and Engineering: A* 589 pp.112-118.
25. Chen, X.-M., Lin, Y. C., Chen, M.-S., Li, H.-B., Wen, D.-X. and Zhang, J.-L. et al. (2015): "Microstructural evolution of a nickel-based superalloy during hot deformation," *Materials & Design*, 77, pp. 41-49.
26. Cao, Y., Di, H., Misra, R., Yi, X., Zhang, J. and Ma, T. (2014): "On the hot deformation behavior of AISI 420 stainless steel based on constitutive analysis and CSL model," *Materials Science and Engineering: A*, 593, pp.111-119.
27. Wang, Y., Shao, W., Zhen, L., Yang, L. and Zhang, X. (2008): "Flow behavior and micro-structures of superalloy 718 during high temperature deformation," *Materials Science and Engineering: A*, 497, pp. 479- 486.
28. Zhang, W. H., Zhang, S. H. (2006): "NiTi alloy hot compress test data correction and constitutive equation." *Journal of Metal.*, 10(42), pp. 69-76.
29. Zhang, J.G., Shi, H.S. and Sun, D.S. (2003): "Research in spray forming technology and its applications in metallurgy." *J Mater Process Technol.*, 138(1-3), pp.357-369.

---

## BINARIZATION FILTERING ALGORITHM FOR VISUAL IMAGE PROCESSING OF MINE INSPECTION ROBOT

Continued from page 282

### Acknowledgement

This work was supported by scientific research project of Hunan Provincial Department of Education "The Application Research in Robot HR20-1700-C10 Vision System Artifacts Sorting" (16C0012).

### References

1. Guo, Weibin and Wang, Hongguang (2012): "A visual servo control system for the robot of the transmission line inspection robot." *Robot*, 34(5), 620-627.
2. Guo, Qi and Hong, Bingrong (2005): "Six DOF space robot is deduced with generalized Jacobi matrix." *The electronic journal*, 2(2), 322-326.
3. Gong, Qing (2002): "A hybrid binarization method for text image." *Journal of Northwest China University of technology*, 20(3), 396-399.
4. Mukhejee, Ranjan and Yoshihiko (2012): "For mulation and efficient computation of Inverse dynamics of space robots." *IEEE Transactions on Robotics and Automation*, 18(3), 400-406.
5. Vasudevan, Shriram K. (2011): "Automotive Image Processing Technique Using Canny' s Edge Detector." *International Journal of Engineering Science and Technology*, 2(7), pp.2632-2643.
6. Xue, Lixia and Li, Tao (2010): "An adaptive Canny edge detection algorithm," *Computer application research*, 27(9), 3588-3590.
7. Zhou, Fengyu and Li, Yibin (2006): "Design of automatic transmission line inspection robot for high voltage transmission line and its inverse kinematic analysis under constraint condition." *China Mechanical Engineering*, 17(1), 4-9.